AGU PUBLICATIONS

JGR

Journal of Geophysical Research: Space Physics

RESEARCH ARTICLE
10.1002/2017JA024936

Key Points:
- Ionospheric topside estimation by Vary-Chap functions
- Spatial and temporal features of the scale height and its gradient
- Global distribution of the topside

Correspondence to:
F. S. Prol,
fabricioprol@hotmail.com

Citation:
Prol, F. S., Hernández-Pajares, M., Camargo, P. O., & Muella, M. T. A. H. (2018). Spatial and temporal features of the topside ionospheric electron density by a new model based on GPS radio occultation data. *Journal of Geophysical Research: Space Physics*, *123*, 2104–2115. https://doi.org/10.1002/2017JA024936

Received 31 OCT 2017
Accepted 8 FEB 2018
Accepted article online 12 FEB 2018
Published online 1 MAR 2018

Spatial and Temporal Features of the Topside Ionospheric Electron Density by a New Model Based On GPS Radio Occultation Data

Fabricio dos Santos Prol[1,2], Manuel Hernández-Pajares[2], Paulo de Oliveira Camargo[1], and Marcio Tadeu de Assis Honorato Muella[3]

[1]Universidade Estadual Paulista-UNESP-Roberto Simonsen, Presidente Prudente, São Paulo, Brazil, [2]UPC-IonSAT, IEEC-CTE-CRAE, Barcelona, Spain, [3]Universidade do Vale do Paraíba-UNIVAP-Laboratório de Física e Astronomia, IP&D, São José dos Campos, São Paulo, Brazil

Abstract A new method for probing the spatial and temporal features of the topside ionosphere is presented. The Vary-Chap model given by linear functions was used to discover and report features of the topside scale height and its gradient. Based on the global coverage of the radio occultation data, spherical harmonic functions were applied to detect some spatial features of the estimated topside. In addition, a Fourier time-dependent method was applied in 10 consecutive years to both estimate and predict the temporal evolution of the topside. As a result, the temporal variation of the peak height showed high correlation with the scale height. And on the other hand, the electron density peak showed a strong anticorrelation with the gradient of the scale height. This suggests that the equatorial topside was mainly controlled by the $\mathbf{E} \times \mathbf{B}$ equatorial vertical drift, which increases the scale height in the equatorial region, and the diffusion of the electrons along the geomagnetic field lines, which reduces the gradient of the scale height. Also, a 1 year prediction with a reasonable accuracy showed that the proposed model can be considered a practical and useful tool for predicting features of the topside ionosphere, which may have special interest for the development of climatological models.

1. Introduction

The development of ionospheric models for describing the topside ionosphere has been a continuous challenge since the discovery of the ionosphere a century ago. One major limitation has remained since the most reliable remote sensing instruments used to explore the topside plasma structure are limited both spatially and temporally, such as the incoherent scatter radars (ISRs) and the topside sounders on board Alouette and ISIS (International Satellites for Ionospheric Studies) satellites. But more recently, the radio occultation (RO) techniques using GPS (Global Positioning System) receivers on board the low Earth orbit satellites are providing continuous data with global coverage of electron density measurements for altitudes above the peak of the ionospheric F_2 layer. Therefore, RO techniques have become an outstanding data source for exploring the topside ionosphere (Liu et al., 2011; Pedatella et al., 2011; Zhao et al., 2011).

During the past decades, several analytical functions have been proposed in order to find a suitable mathematical formulation that describes the altitude dependence of the electron density in the topside, such as exponential functions (Llewellyn & Bent, 1973; Stankov et al., 2003), parabolic functions (Kutiev & Marinov, 2007), Epstein functions (Depuev & Pulinets, 2004; Radicella & Leitinger, 2001; Rawer, 1988), and Chapman functions (Chapman, 1931; Reinisch et al., 2004; Venkatesh et al., 2011). Fonda et al. (2005), for instance, presented a comparison between distinct analytical functions and found that the Chapman model best described the topside ionosphere when compared to the topside sounder observations. As a result of the Chapman adjustment, one of the most important parameters that describes the ionospheric characteristics is estimated—the scale height. In general, the scale height is defined as the vertical distance over which the electron density diminishes by a factor of e and can be used as a measure of the ionospheric density gradient (Marinov et al., 2015) and ionospheric slab thickness (Duarte-Silva et al., 2015). But in addition, it shows a dependence with the thermal structure and composition of the ionosphere, which might contribute to describe ionospheric features that are not completely understood.

There are various numerical ways to compute the scale height using the Chapman functions. Often, a simplifying assumption is made to represent the topside by an α-Chapman function with constant scale height (Reinisch et al., 2004), that is, a unique scale height is estimated for the entire topside. In order to incorporate an altitude dependence on the scale height, Rishbeth and Garriott (1969) first proposed a formulation considering a continuously varying scale height, which was later named Vary-Chap. Reinisch et al. (2007) used a hyperbolic tangent function to fit the proposed Vary-Chap to ISIS sounders, and it became a presumable option to improve the topside profiles of the International Reference Ionosphere (IRI) (Bilitza et al., 2011). Such task faces mainly a limitation due to the lack of data measured by a large number of instruments around the globe, which could be improved by the incorporation of RO observations.

Current studies are revealing that Chapman functions are performing well to describe the topside ionosphere retrieved by the RO data. The validation of the scale height derived from RO has been presenting good agreements with the vertical total electron content (Wu et al., 2016), as well as consistent seasonal variations and strong dependence on temperature (Stankov & Jakowski, 2006). Most of the studies retrieving the topside by RO were carried out using a fixed scale height. On the other hand, Olivares-Pulido et al. (2016) and Hernández-Pajares et al. (2017) have found that the RO electron density observations above the peak fit much better to a varying scale height described by a linear dependence, where two parameters can be estimated to better describe the ionosphere topside above the peak height, h_m, and bellow the low Earth orbit height: the scale height at h_m and the gradient of the scale height.

Despite the considerable efforts already made to describe the topside ionosphere, a relevant challenge still remains due to the lack of information on the global patterns of the topside ionosphere when described by Vary-Chap functions retrieved by RO data. In this regard, we are taking the advantage of the global coverage of RO data to analyze spatial and temporal patterns of the topside ionosphere using a new technique for estimating the linear Vary-Chap. Therefore, a pioneering set of procedures is presented to discover and report global features of the spatial and temporal behavior of the topside scale height and its gradient. The electron density and height at the F_2 peak are also analyzed in order to give a complete view of the Vary-Chap topside. They were obtained from the Constellation Observing System for Meteorology, Ionosphere, and Climate (COSMIC) Data Analysis and Archive Center and processed by UCAR (University Corporation for Atmospheric Research) following the methods developed by Schreiner et al. (1999) and Syndergaard et al. (2005). As a result, the first section shows how the ionospheric profiles were independently used to retrieve the topside. A spatial modeling was then carried out to show the spatial patterns of the peak height, electron density peak, scale height, and its gradient. At last, a time modeling was performed to describe the temporal evolution of the estimated values and the possibility of their prediction.

2. New Procedure to Estimate the Vary-Chap Function

The topside of the ionosphere was represented by the Vary-Chap functions, which characterizes the topside by an exponential decay with altitude. The general Vary-Chap function is a simple mathematical formulation that describes the electron density profile with a scale height H_s (that varies with height h) by the following equation:

$$N_e(h) = N_m e^{k(1-z-e^{-z})} \quad with \quad z = \frac{h - h_m}{H_s(h)} \tag{1}$$

where N_e is the electron density at the height h, N_m and h_m are the density and height at the F_2 peak, $k = 1/2$ for the α-Chapman function, and $k = 1$ for β-Chapman.

Olivares-Pulido et al. (2016) have found that linear functions can be used to well estimate the variability of the scale height at the topside when adjusted to RO data, finding the Pearson coefficient above 0.98 for more than 72% of the analyzed RO ionospheric profiles. In this regard, the varying scale height is approximated as the following linear equation:

$$H_s(h) = \frac{\partial H_0}{\partial h}(h - h_m) + H_0 \tag{2}$$

where H_0 stands for the scale height referred to the peak height and $\partial H_0/\partial h$ to the gradient of H_0. In Olivares-Pulido et al. (2016), a two-step procedure was applied to the determination of H_0 and $\partial H_0/\partial h$. First, z was iteratively obtained based on electron density data, and second, a fitting of the linear function given by equation (1) was carried out.

The main difference of the method proposed in this work is that the electron density observations are directly used for the estimation of H_0 and $\partial H_0/\partial h$. Here a linear least square method based on equation (1) is used, where $H_s(h)$ was approximated by equation (2), that is, $H_s(h) = \partial H_0/\partial h(h-h_m)+H_0$. The following steps were considered for the estimation:

Step 1: Exclusion of N_e outliers and construction of the measurement vector $\boldsymbol{y}$;
Step 2: Initialize the vector of approximated parameters $\boldsymbol{x}_0$ using $H_0^o = 80$ km and $\frac{\partial H_0^o}{\partial h} = 0.1$;
Step 3: Use H_0^o and $\frac{\partial H_0^o}{\partial h}$ in equation (1) to obtain the vector of approximated measurements $\boldsymbol{y}_0$;
Step 4: Build the Jacobian matrix $\boldsymbol{H}$ using equations (3) and (4) shown ahead;
Step 5: Obtain the vector of the estimated parameters by $\boldsymbol{x} = \boldsymbol{x}_0 + (\boldsymbol{H}^T\boldsymbol{H})^{-1}\boldsymbol{H}^T(\boldsymbol{y}-\boldsymbol{y}_0)$;
Step 6: Update the initial parameters of H_0^o and $\frac{\partial H_0^o}{\partial h}$ by $\boldsymbol{x}_0 = \boldsymbol{x}$;
Step 7: Go to Step 3 if the number of iterations is smaller than 20 times. Otherwise, end the iterations.

The Jacobian matrix is given by the following partial derivatives:

$$\frac{\partial N_e}{\partial H_0} = kN_m\left[\frac{(h-h_m)}{(H_s^o)^2} - \frac{(h-h_m)e^{-z^o}}{(H_s^o)^2}\right]e^{k(1-z^o-e^{-z^o})} \tag{3}$$

and

$$\frac{\partial N_e}{\partial(\partial H_0^o/\partial h)} = kN_m\left[\frac{(h-h_m)^2}{(H_s^o)^2} - \frac{(h-h_m)^2e^{-z^o}}{(H_s^o)^2}\right]e^{k(1-z^o-e^{-z^o})} \tag{4}$$

where z^o and H_s^o are obtained using approximated values of H_0^o and $\partial H_0^o/\partial h$. In general, the adjustment process converges well with a low number of iterations. However, when nonreal values are obtained, such as negative values of H_0^o, $H_0^o > 1,000$ km or $\partial H_0^o/\partial h > 1$, the estimation process is reinitialized with H_0^o or $\partial H_0^o/\partial h$ equal to twice or half the number used before, depending if the estimated values are above or below the thresholds.

Figure 1 (left) shows a typical example of the performance of the proposed method. It shows a profile of observations derived from measurements of the ISR at Millstone Hill, the profile retrieved when fitting a constant scale height and the profile retrieved when fitting the varying scale height with the proposed method, referred as Vary-Chap. ISR data were used in this example due to the important measurements of the ionospheric temperature that it provides, in addition to the electron density. The data set was obtained from the final data processed in a campaign of measurements available in Madrigal database that were conducted to obtain reliable data of the atmospheric warming on 15 January 2010. As can be seen, the varying scale height is more flexible to describe the topside due to the strong influence of the gradient in the upper part of the topside, which includes a considerable improvement when compared to the fixed scale height. In fact, both α-Chapman and β-Chapman could lead to the same result in terms of the estimated electron density; however, considerable differences in the magnitude of the estimated values of H_0 and $\partial H_0/\partial h$ are obtained when using these approaches. In order to identify the best option for the topside estimation, H_0 and $\partial H_0/\partial h$ were estimated using α-Chapman and β-Chapman functions and compared to the scale height calculated through temperature measurements of ISR. As pointed out by Belehaki et al. (2006), the scale height derived from Chapman functions can be theoretically evaluated by the neutral temperature. Therefore, the scale height from ISR measurements was derived using the following equation:

$$H_s = \frac{k_b\,T_n}{m(O)\,g} \tag{5}$$

where T_n is the neutral temperature, k_b is the Boltzmann's constant (1.38×10^{-23} m^2 kg s^{-1} K^{-1}), $m(O)$ is the oxygen mass (2.65×10^{-26} kg), and g is the acceleration of gravity (9.81 m s^{-2}).

Figure 1 (top right) shows the estimated value of $H_s(h)$ for a fixed height of 520 km over almost 6 h of data. It is presented H_s from the proposed iteration process with $k = 1$, the proposed process with $k = 0.5$ and derived from equation (5). Also, Figure 1 (bottom right) shows the gradient of the scale height ($\partial H_0/\partial h$). This experiment was performed to make a preliminary check whether the magnitude of the topside estimated by the proposed procedure was close to the scale height derived from temperature measurements. In general, both Vary-Chap functions presented similar values of the scale height and its gradient in comparison to the ISR values. In this respect, the magnitude of the estimated values of the proposed method seems reliable. In addition, a better agreement was clearly obtained for the α-Chapman function in comparison to the scale height derived from ISR. The mean difference between the ISR H_s and the Vary-Chap H_s

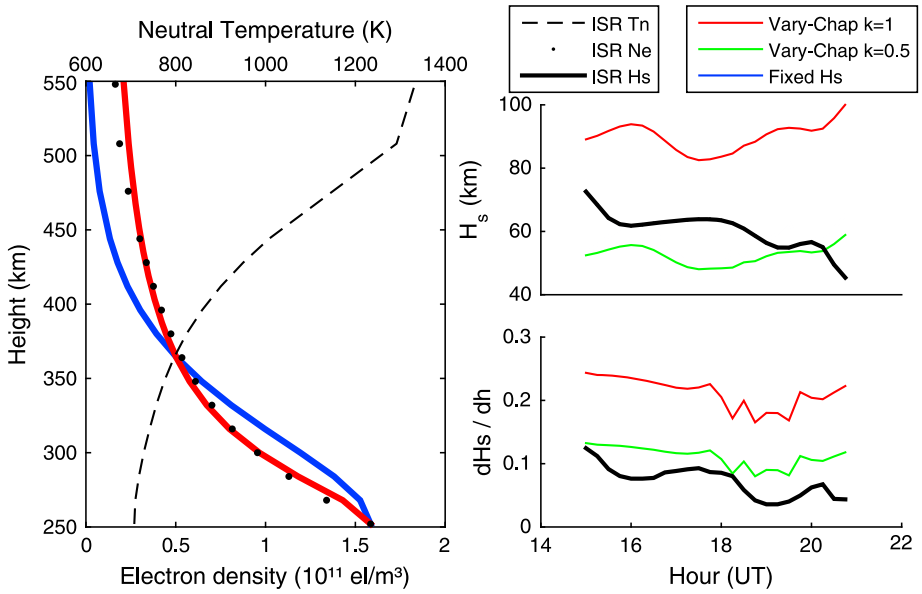

Figure 1. The left panel shows the topside estimation using a fixed scale height (blue line) and a varying scale height with $k = 1$ (red line) and $k = 0.5$ (green line). The black dots are the N_e observations obtained from ISR data. The panels on the right show the estimated values of H_s (top) and $\partial H_0/\partial h$ (bottom) for 6 h of data. The black line of the top right panel was obtained using equation (5) for an altitude of 520 km. The green and red lines are the scale height H_s obtained from the proposed iteration process. The ISR gradient $\partial H_0/\partial h$ is the average of the gradients obtained using all observations above the peak height.

using $k = 1$ was 29 km, while the mean difference using $k = 1/2$ was 9 km, with the later being the one that best describes the ionospheric topside. Consequently, the subsequent analyses were performed using the α-Chapman function.

The reliable magnitude of the values estimated with the proposed procedure when compared to ISR data, among the lack of studies that shows the dynamics of the scale height and its gradient, inspired us to check the spatial and temporal patterns of the estimated H_0 and $\partial H_0/\partial h$. Such analyses were carried out using RO data in order to obtain a global coverage and reasonable amount of data from consecutive days. We were also interested in the spatial and temporal patterns of h_m and N_m to show whether the RO data were reliable to estimate the expected patterns of h_m and N_m and then to obtain the correlations between the parameters. Therefore, after applying the topside estimation procedure for independent RO profiles, four parameters, h_m, N_m, H_0, and $\partial H_0/\partial h$, were recorded with the horizontal position related to the coordinates of the peak height.

3. Spatial Modeling

In order to process the spatial interpolation of h_m, N_m, H_0, and $\partial H_0/\partial h$ and represent global patterns of these parameters, RO data of close days and hours were superimposed in a Sun-fixed reference frame. Figure 2 shows an example of the spatial distribution of N_m converted to the critical frequency (*foF2*) superimposed with distinct number of consecutive days of RO data in terms of local time (LT) and magnetic latitude. The conversion of the electron density peak (in el/m^3) into critical frequency (in MHz) was computed by $foF2 = \sqrt{N_m/(1.24 \times 10^{10})}$, and the data were obtained from the FORMOSA Satellite Series No. 3 (FORMOSAT-3)/COSMIC (Lei et al., 2007). In general, the best coverage was obtained when all data of 60 consecutive days between days of year (hereinafter as DOYs) 70 and 130 of 2017 were superimposed; that is, a window of 30 days better depicted the ionosphere at the central DOY 100. The RO data used in this study were given by COSMIC Data Analysis and Archive Center and processed by UCAR. It is worth mentioning that when analyzing all the RO data obtained between the years of 2008 and 2017, we have found that a 30 day window is good enough to provide, for any specific day, a global distribution without gaps that could affect the spatial modeling of the parameters.

The spatial modeling was performed using spherical harmonics (SH) expansion, which are mathematical functions widely used to represent the behavior of several atmospheric parameters at a global scale.

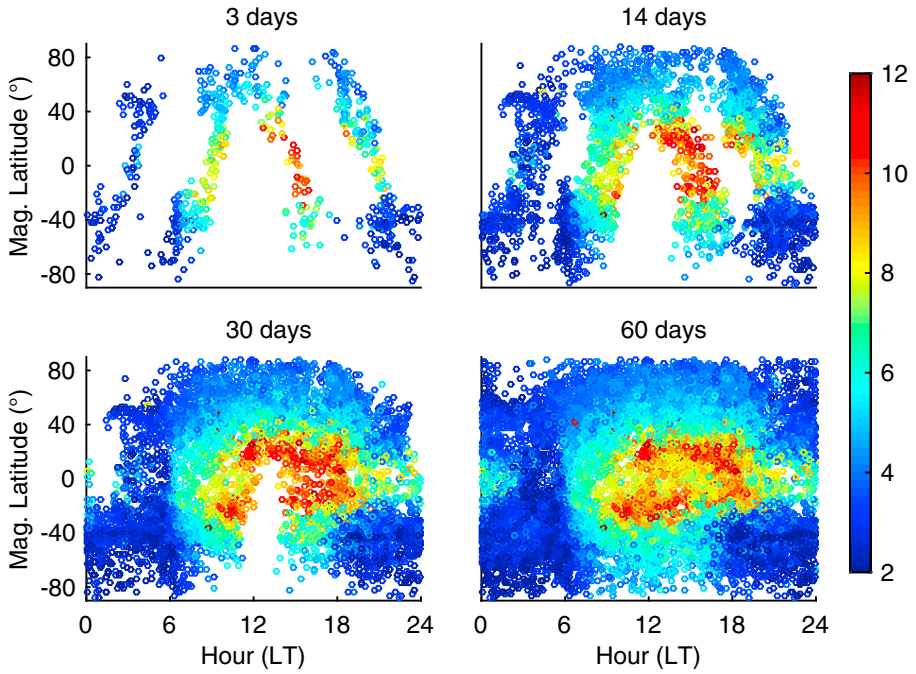

Figure 2. Coverage of FORMOSA Satellite Series No. 3/Constellation Observing System for Meteorology, Ionosphere, and Climate radio occultation data when varying the number of consecutive days with superimposed data of N_m. The unit of the color bar is megahertz, and the central day of each global representation was day of year 100 of 2017.

The parameters h_m, N_m, H_0, and $\partial H_0/\partial h$ were spatially represented by a set of coefficients given by the following equation:

$$f(\phi_m, t_L) = \sum_{n=0}^{N} \sum_{m=0}^{n} P_{nm}(\sin \phi_m) \left[a_{nm} \cos\left(\pi \frac{m t_L}{12}\right) + b_{nm} \sin\left(\pi \frac{m t_L}{12}\right) \right] \quad (6)$$

where $f(\phi_m, t_L)$ stands for any of the target parameters, ϕ_m is the magnetic latitude, t_L is the LT, P_{nm} is the normalized associated Legendre polynomial, and a_{nm} and b_{nm} are the coefficients to be determined in a least square adjustment with degree $N = 15$, which give us 256 coefficients to be estimated for each parameter.

Figure 3 shows the resulting surfaces of h_m, N_m, H_0, and $\partial H_0/\partial h$ when applying the SH estimation in three representative days of the minimum in the solar cycle 24: northern solstice (DOY 172), equinox (DOY 264), and southern solstice (DOY 356) of 2008. It is also presented the scale height computed by equation (5) using the neutral temperature derived from IRI-2012 for a fixed height of 400 km and the scale height H_1, which is the scale height at a fixed height of 400 km computed by $H_1 = H_0 + \partial H_0/\partial h\ (400 - h_m)$. Figure 4 shows the same configuration, but for the year 2014, which was a maximum in the solar cycle 24. It is possible to see the expected global patterns of N_m, such as the representation of the two crests of the equatorial ionization anomaly (EIA). It is also noticed an asymmetric behavior, where the north crest is more intense when the summer Sun is located in the Northern Hemisphere and the south crest is more intense when the summer Sun is located in the Southern Hemisphere. In addition, the h_m estimation is presenting an expected surface of the peak height, with higher values in the equatorial region, where the electron density distribution is driven by the resulting force due to the electric and geomagnetic fields in the ionosphere. The daytime and nighttime of both surfaces of N_m and h_m are clearly defined, and the values were estimated with reasonable magnitude, which follows an increasing trend together with the solar cycle. Therefore, it is reasonable to say that the proposed SH estimation procedure using the RO data provides consistent global patterns of the ionospheric topside.

Some interesting features can be verified in the estimated spatial distributions of H_0, which were obtained with similar magnitude as in previous works (Liu et al., 2011; Olivares-Pulido et al., 2016) and with similar magnitude of H_s derived from the neutral temperature of IRI (H_{IRI}). A similar consistency of H_0 and H_1 was obtained, with small differences due to the contribution of $\partial H_0/\partial h$. Also, the H_0 surface clear follows H_{IRI} and the position

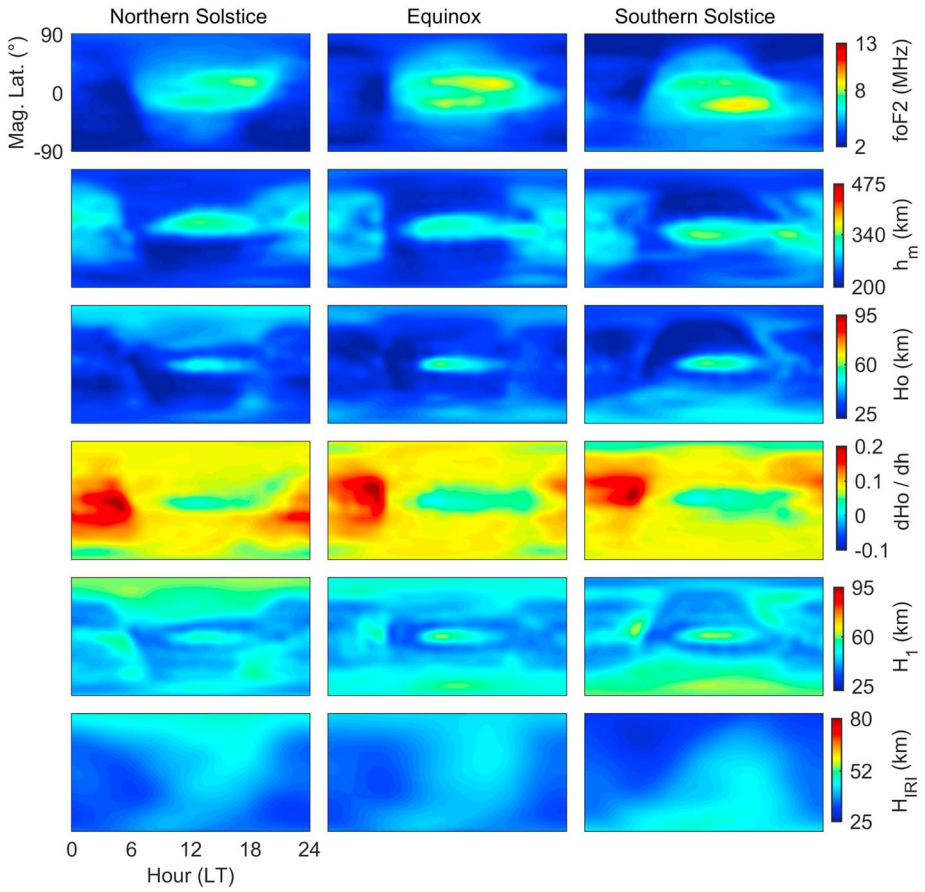

Figure 3. Spatial patterns of h_m, N_m, H_0, and $\partial H_0/\partial h$ for distinct periods of solstices and equinoxes in the year 2008. It is also shown the scale height derived by the neutral temperature of the ionosphere and computed from International Reference Ionosphere 2012 model.

of the Sun, showing higher values in the Northern Hemisphere during the northern solstice (June), higher values in the Southern Hemisphere during the southern solstice (December), and a balanced behavior in the equinox. In the hemisphere that corresponds to the solstices, the H_0 values are higher in the daytime and lower at nighttime. There is also a lower daily variation of H_0 in the polar region during the solstices, which is mainly due to the absence of dark nights. Therefore, it seems that the spatial distribution of the estimated H_0 is closely related to the ionospheric temperature patterns, which are mainly driven by the solar irradiation. However, there are two important patterns that are not well explained by only looking to the Sun position and the temperature patterns of H_{IRI}. First, there are high values of H_0 in the equatorial region in the daytime that appears to be independent of the position of the Sun, and second, there is a noticeable lower concentration of H_0 in low latitudes and midlatitudes in the daytime for the regions in the winter, that is, in the Southern Hemisphere during the northern solstice (June) and in the Northern Hemisphere during the southern solstice (December).

Over the geomagnetic equator, the electric and magnetic fields are mutually perpendicular to each other. The resulting force in the daytime drives the electron density to higher altitudes with a drift velocity $\mathbf{E} \times \mathbf{B}$, where **E** and **B** stand for the vectors of the electric and geomagnetic field. It is well known that the peak height is correlated to the intensity of the electric currents at the equator. However, in addition to this, the results of Figures 3 and 4 indicate that not only the peak height changes with the resulting vertical drift but also a higher concentration of electrons in the upper ionosphere has changed the shape of the topside by increasing H_0. Indeed, the higher values of H_0 seem even more confined to the equator than the h_m distributions, which is an indication that H_0 might be more affected by the intensification of the vertical drift in the equatorial region than h_m. This may be true because the increasing of h_m depends on the elevation of the entire F_2 layer, while H_0 increases only by having a few more electrons in the upper part.

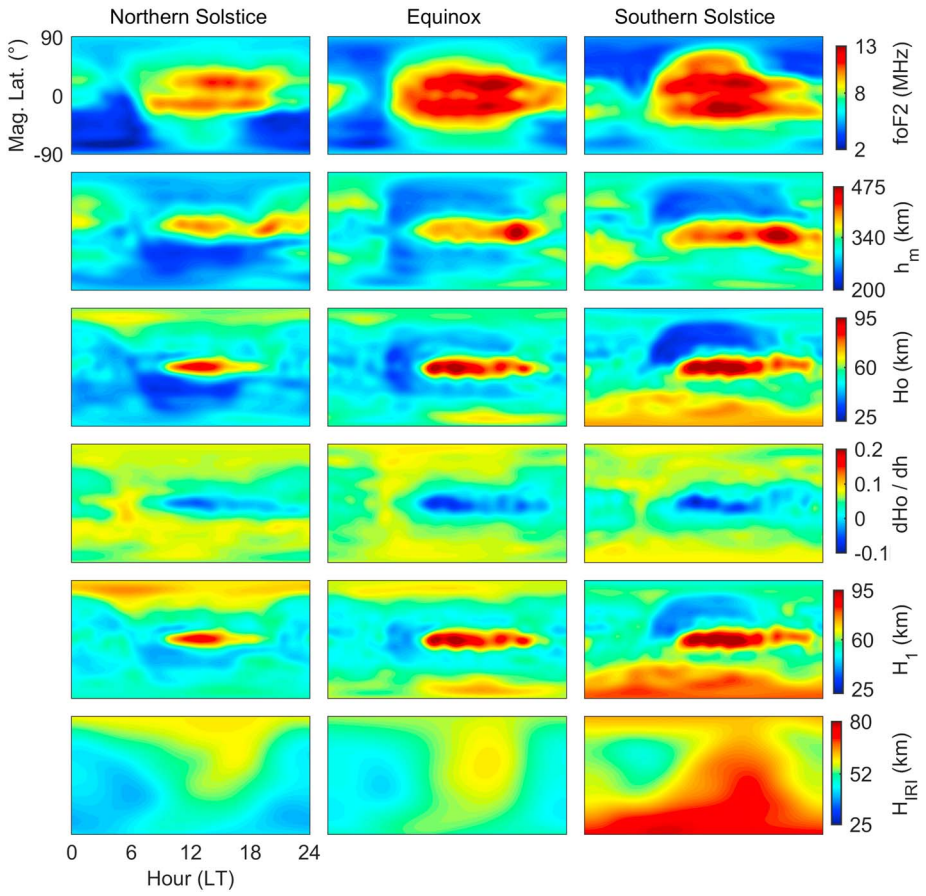

Figure 4. Spatial patterns of h_m, N_m, H_0, and $\partial H_0/\partial h$ for distinct periods of solstices and equinoxes in the year 2014. It is also shown the scale height derived by the neutral temperature of the ionosphere and computed from International Reference Ionosphere 2012 model.

Figure 5 illustrates the synergy between the vertical drift at the equatorial region, driven by $\mathbf{E} \times \mathbf{B}$ force, and real profiles obtained with the estimated h_m, N_m, H_0, and $\partial H_0/\partial h$. Despite lower values of N_m in the geomagnetic equator than N_m of low-latitude regions, it is possible to see a higher concentration of electron density above the peak height of the equator, mainly for the altitudes between 500 km and 700 km. Such higher electron density is the main cause of an increasing of H_0 in the geomagnetic equator. In addition, it is interesting to note that at higher altitudes, the uplifted plasma diffuses along with the geomagnetic field lines in the direction to the low-latitude regions, forming the crests of EIA by the so-called fountain effect. Therefore, there is a continuous flow of electrons that are leaving the upper part of the equatorial topside. But instead of reducing the values of H_0, the parameter that is mainly affected by the diffusion of the electrons is the gradient $\partial H_0/\partial h$. In this regard, despite the electron density being higher in the topside of the equatorial profile, the exponential decay with the altitude is not so strong in the equatorial region when compared to the low-latitude profiles. Indeed, $\partial H_0/\partial h$ mainly controls how strong is the exponential decay of the electron density in the upper part of the topside. Therefore, there is an anticorrelation between H_0 and $\partial H_0/\partial h$ observed in the equatorial region in Figures 3 and 4 that can be mainly associated with the vertical drift, which increases H_0, and a diffusion of the electrons along the geomagnetic field lines, which reduces the values of $\partial H_0/\partial h$.

The electron density that diffuses along with the geomagnetic field lines toward the crests of EIA remains mainly in the peak height h_m. The fountain effect, therefore, contributes to a considerable increasing of the electron density in the peak height of the crests of EIA. However, during the fountain effect, the topside of the crests does not show significant changes. In this sense, the increasing of N_m linked to the low variability of the topside indicates that it is reasonable to observe lower values of H_0 in the crests of EIA, mainly in the winter, since the peak height is lower at this season.

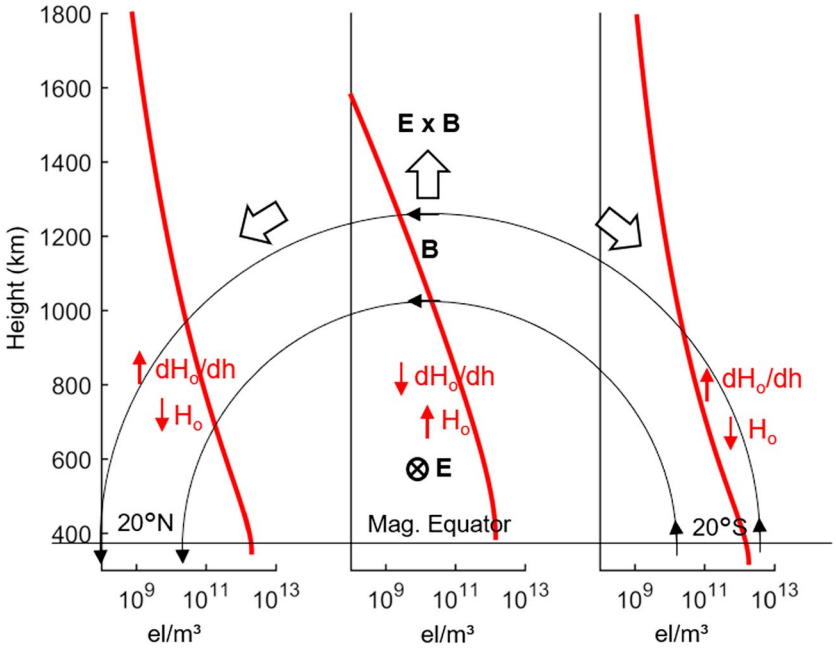

Figure 5. Topside variability of the profiles due to the ionospheric fountain effect. The electron density is plotted on a logarithmic scale.

It is important to observe a relevant increase of the equatorial $\partial H_0/\partial h$ after 00 LT and a further increasing near 05 LT in Figures 3 and 4. During nighttime, the recombination process quickly reduces the electron density of the ionosphere near the peak height. On the other hand, the plasma at higher altitudes is maintained due to the low recombination rates. In addition, the electron density at the plasmasphere can flow back into the *F* region on the night, as mentioned by Kelley (2009). Therefore, since $\partial H_0/\partial h$ is strongly controlled by the electron density at the upper part of the topside, the high values after 00 LT is likely related to the variations due to the topside recombination process and the plasmasphere. Also, the $\partial H_0/\partial h$ increasing near 05 LT can be also related to the local sunrise. At the local sunrise, the sunlight reaches first the upper part of the topside. The increasing of the ion production in the upper part of the topside raises the electron density, but no significant variation occurs at the peak height. Consequently, there is a justifiable increasing of $\partial H_0/\partial h$. Such event was also indicated in Prol and Camargo (2016) as the main reason that was affecting the estimation of N_m by the ionospheric tomography. But at that time, the electron density increasing of topside in the local sunrise was only a speculation that now can be seen thanks to the proposed model based on RO data.

4. Time Modeling

The SH coefficients for all the days between the beginning of the year 2008 and the end of 2015 were estimated with a moving window of 30 days. A temporal series was then obtained for each SH coefficient, which enabled to analyze the temporal dependence of the coefficients. Figure 6 (top) shows the time dependency of the first SH coefficient (a_{00}) obtained from the observations of N_m, converted to the critical frequency. It is also presented the behavior of the solar activity given by the solar radio flux at 10.7 cm (F10.7 index) and a global view of the ionosphere given by the global electron content (GEC) derived from the UPC Quarter an hour Rapid GIM global ionospheric maps produced by Universitat Politècnica de Catalunya (Hernández-Pajares et al., 1999). Each daily value was divided by the mean value of the time series in order to show a superimposed graphic. Despite that the time series were obtained from distinct instruments and distinct processing techniques, it is possible to see a good agreement between N_m (in el/m^3), F10.7 (in units of 10^{-22} W m^{-2} Hz^{-1}), and GEC (in units of 10^{32} electrons). The correlation of N_m and F10.7 was 91% and of N_m and GEC was 96%, which indicates the consistency of the proposed method in order to analyze the global behavior of the ionosphere.

A fast Fourier transform (FFT) algorithm was used before applying a time modeling procedure in the time series given by 256 SH coefficients for each of h_m, N_m, H_0, and $\partial H_0/\partial h$. FFT was applied to convert the time domain of the SH coefficients to a representation in the frequency domain and then identify the periods

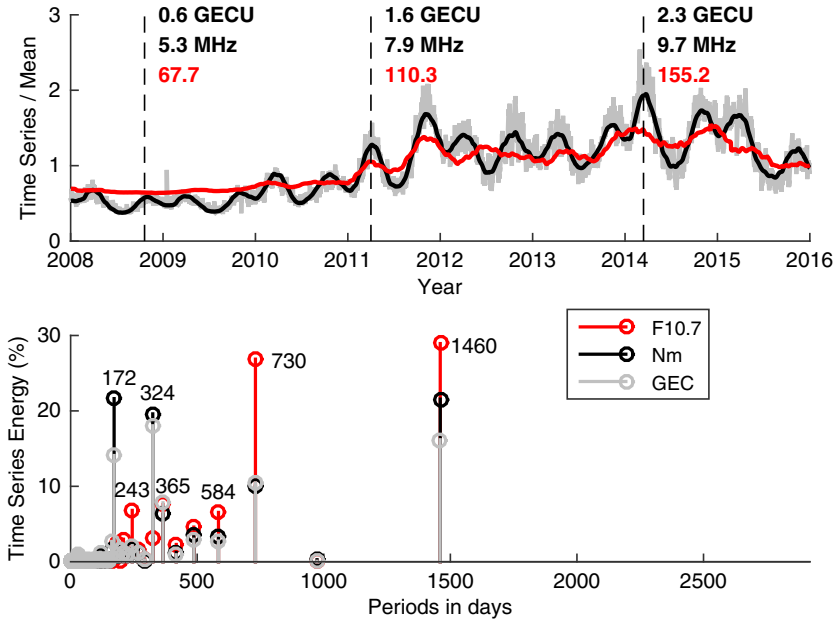

Figure 6. The top panel shows the time series of the first spherical harmonics coefficient of N_m, converted to megahertz, the corresponding values of the 81 day running mean of the F10.7 index and global electron content (GEC) in GEC units (GECU), where 1 GECU = 10^{32} electrons. The bottom panel shows the periods detected by FFT with high energy in the time series.

that shows predominant temporal patterns. The frequencies that contribute the most to the time series were identified using a specific criterion. We used the frequencies that were capable of showing at least 99% of the energy of the time series, where Figure 6 (bottom) shows the identification of the frequencies, converted to periods, that contributed the most to the first coefficient of N_m. It is also represented the predominant periods obtained when applying the FFT to the time series of F10.7 and GEC, showing that the time series have similar temporal patterns. In general, it is possible to verify that higher energies of the first coefficient of N_m, F10.7 and GEC are mainly related to the periods of 1,460 days (4 years), 730 days (2 years), and 365 days (1 year). There were also two periods given by 172 and 324 days with high energy of N_m and GEC, but low energy of the F10.7 solar flux index, as expected, since F10.7 in an indicator of the solar activity. Therefore, seasonal patterns of the ionosphere, mainly due to the regional variations in the Northern and Southern Hemispheres, lead to a better agreement between GEC and N_m. It is relevant saying that despite showing results of N_m, similar principal periods of the temporal patterns were detected for the coefficients of h_m, H_0, and $\partial H_0/\partial h$.

After calculating the most important time-dependent periods of each SH coefficient, a time modeling procedure was carried out. The temporal modeling of h_m, N_m, H_0, and $\partial H_0/\partial h$ was described by a Fourier time-dependent method. In this regard, the time series of a specific SH coefficient was approximated in Fourier coefficients by the following equation:

$$a_{nm}^{(08\ldots15)} = c_0 + \sum_{n=1}^{N} c_n \sin\left(2\pi \frac{t_d}{T_d^{(n)}}\right) + d_n \cos\left(2\pi \frac{t_d}{T_d^{(n)}}\right) \tag{7}$$

where $a_{nm}^{(08\ldots15)}$ is the time series of a specific SH coefficient related to the years between 2008 and 2015, c_n and d_n are the Fourier coefficients to be estimated, t_d is the day of the time series varying from 1 to 2920, and $T_d^{(n)}$ is the period of the sinusoidal function, which depends on the value of n and was defined by the most important frequencies obtained in the FFT analysis. The Fourier series of equation (7) was expanded up to N, which represents the number of needed frequencies to describe at least 99% of the energy of the time series. In addition to the FFT periods, it was included the period of 4,017 days, which represents the entire solar cycle that was not detected by FFT due to the small size of the data set.

Figure 7 shows the performance of the Fourier fitting when applied to the first coefficient of the time series of h_m, N_m, H_0, and $\partial H_0/\partial h$. It also shows the predicted values of the coefficients by extending the Fourier adjustment to the whole year of 2016 and 150 days of 2017, covering all data available nowadays

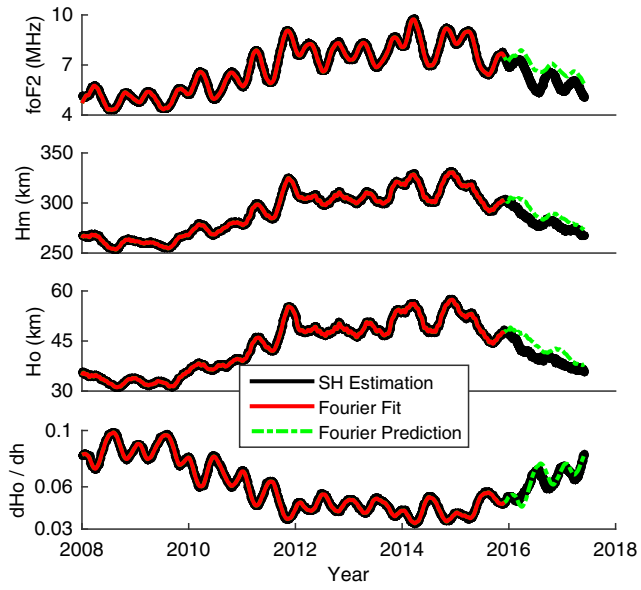

Figure 7. Temporal evolution of h_m, N_m, H_0, and $\partial H_0/\partial h$ calculated trough a moving window of 30 days using the spherical harmonics (SH) estimation, the Fourier adjustment, and the Fourier prediction.

from FORMOSAT-3/COMISC for the solar cycle 24. In this example, the SH estimation was also applied for 2016 and 2017 with a moving window of 30 days to show reference values to the prediction. As can be seen, the Fourier fitting performed well to describe the first SH coefficients between 2008 and the end of 2015. Despite a small worsening, the Fourier had either a reasonable or good performance in the prediction for 2016 and 2017, which indicates that the detected periods from FFT described well the energy of the time series.

From the results of the prediction, it can be said that the estimated coefficients of h_m, N_m, H_0, and $\partial H_0/\partial h$ have predictable temporal patterns, so it gives strong indications that physical interpretations can be associated with them. In general, the anticorrelation of H_0 and $\partial H_0/\partial h$ does not occur occasionally for the spatial distributions between equinox and solstices, such as observed in the previous section, but there is also a temporal evolution of the parameters that conduct to an anticorrelation. However, in the case of the temporal patterns, it can be seen in Figure 7 that the gradient of the scale height is highly anticorrelated with N_m. The obtained anticorrelation between the time series of N_m and $\partial H_0/\partial h$ was −94%. This high anticorrelation can be explained because, as mentioned before, the gradient $\partial H_0/\partial h$ in the equatorial region is likely controlled by the decrease in the electron density in the topside due to the plasma fountain effect, while N_m increases in the crests due the diffusion of the electron density along with the geomagnetic field lines. Therefore, despite a spatial distribution of $\partial H_0/\partial h$ completely distinct in comparison to the spatial distributions of N_m, when we look to the global mean values, that is, the first SH coefficient, we can notice that they are highly correlated. Other ionospheric regions than the equatorial contributes to the first SH coefficient, but we are mainly looking to the equatorial region and the crests of EIA because they play the most principal role. It is interesting to notice that the H_0 temporal evolution

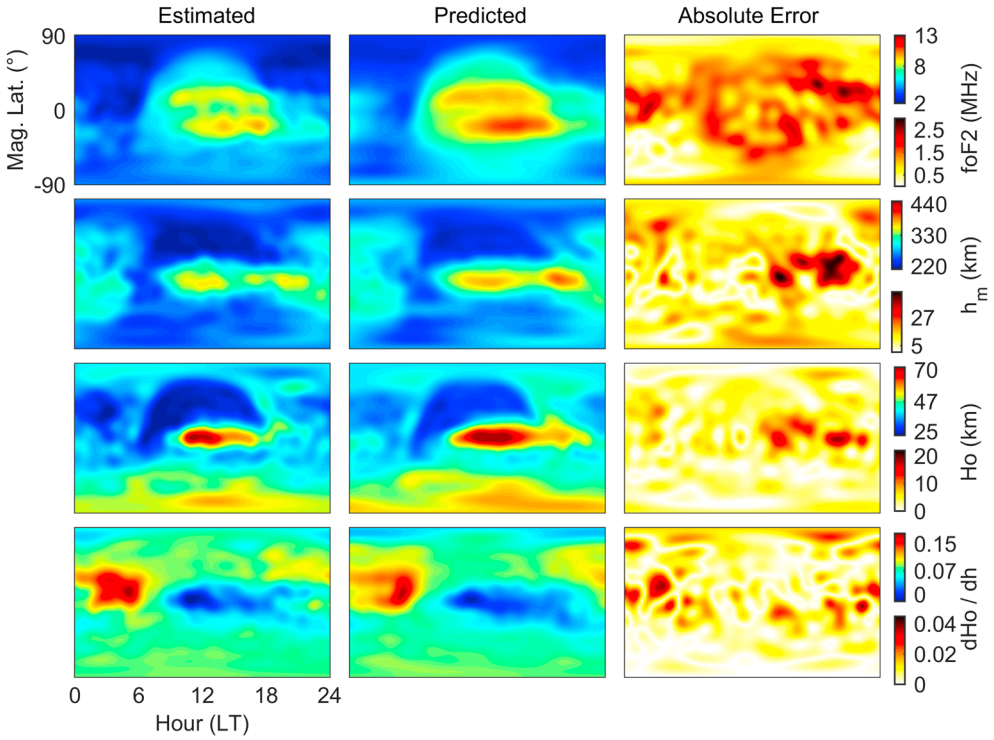

Figure 8. Comparison between the surfaces obtained with the spherical harmonics estimation and the Fourier prediction on day of year 356 of 2016 (Southern Solstice). The last observation used for the prediction is from day of year 365 of 2015.

is quite closely related to the h_m temporal evolution. Indeed, the correlation between the time series of H_0 and h_m was 99%. This is mainly because, as mentioned before, both parameters are controlled by the equatorial currents that drift the electron density at the equatorial region to higher altitudes.

In order to analyze all the estimated and predicted SH coefficients, Figure 8 shows the distribution in geomagnetic latitude and LT obtained for h_m, N_m, H_0, and $\partial H_0/\partial h$ when the proposed method was applied in DOY 356 of 2016 (southern summer solstice). This is a representative example because it shows the performance of the prediction when applied to almost 1 year after the last observations was incorporated into the Fourier estimation, which is a relevant challenge in terms of the prediction. The prediction was capable of showing the Seasonal patterns, being H_0 higher in the Southern Hemisphere and N_m more intense in the southern crest of the EIA. It has also shown lower values of h_m and H_0 in the Northern Hemisphere, a clear spatial anticorrelation between H_0 and $\partial H_0/\partial h$ in the equatorial region, as well as the $\partial H_0/\partial h$ increasing at 05 LT, mainly due the local sunrise. However, despite the possibility to predict seasonal patterns, some regional structures were smoothed, which produced nonnegligible errors. The root-mean-square error (RMSE) and maximum absolute error was 1.1 and 2.7 MHz for *foF*2, as calculated from N_m, 14.1 and 47.0 km for h_m, 4.5 and 18.6 km for H_0, and 0.01 and 0.04 for $\partial H_0/\partial h$. By taking the ratio of the maximum error and the maximum estimated value, we computed the magnitude error of 47%, 13%, 25%, and 22% for N_m, h_m, H_0, and $\partial H_0/\partial h$. These results indicate that in general, the magnitude of the prediction is in a good agreement with the estimated reference value and that the N_m parameter was the most difficult to predict. Also, bearing in mind that this evaluation is constrained to the coefficient domain of the SH functions, we also calculated the RMSE for all RO ionospheric profiles in DOY 356 of 2016, that is, the reference values were derived from each RO profile without any SH interpolation. As a result, the obtained RMSE was 1.5 MHz for *foF*2, 30.4 km for h_m, 13.1 km for H_0 and 0.03 for $\partial H_0/\partial h$, which is a bit worse result than the SH constrained assessment but still in a good agreement. Therefore, spatial patterns and the magnitude of all parameters can be predicted with a reasonable accuracy, which is a clear indication of the applicability of the climatological model developed in this study to the estimation of the topside ionospheric parameters based on RO data.

5. Conclusions

We have successfully implemented a procedure to estimate spatial and temporal patterns of the varying scale height of the topside ionosphere (H_0) and its gradient ($\partial H_0/\partial h$) as well as the electron density (N_m) and height (h_m) at the F_2 peak. All RO data available from FORMOSAT-3/COSMIC from the solar cycle 24, which corresponds to 10 consecutive years between 2008 and 2017, were used for probing some features of the estimated parameters. Thus, simultaneous analysis of these parameters provided new information about the topside ionosphere.

The obtained results can be summarized as follows:

1. It is possible to analyze the spatial features of h_m, N_m, H_0, and $\partial H_0/\partial h$ by using RO data as well as predict their values to show temporal patterns.
2. The global patterns of the electron density peak obtained with RO data are highly correlated with the GEC derived from global ionospheric maps.
3. The temporal evolution of the global mean of H_0 is highly correlated with h_m, and the temporal evolution of the global mean of $\partial H_0/\partial h$ has a strong anticorrelation with N_m.
4. When describing the topside by a linear Vary-Chap, we find a spatial anticorrelation in the equatorial region between H_0 and $\partial H_0/\partial h$.
5. The estimated ionospheric profiles indicate that the anticorrelation between H_0 and $\partial H_0/\partial h$ is mainly associated with the equatorial vertical drift, which increases H_0, and with the diffusion of the electrons along the geomagnetic field lines, which reduces the values of $\partial H_0/\partial h$.
6. There is an increasing of $\partial H_0/\partial h$ near 05 LT which is mainly associated with the increasing of the ion production in the topside due to the solar irradiation that first reaches the upper part of the topside in the local sunrise.
7. The performance of the proposed model applied for one year of prediction showed a good agreement with the reference values. The prediction showed well the seasonal features of the topside and was performed with an RMSE of 1.1 MHz for N_m, 14.1 km for h_m, 4.5 km for H_0, and 0.01 for $\partial H_0/\partial h$, which reveals the GPS RO as a powerful instrument to build climatological models for the topside ionosphere.

Acknowledgments
This work was jointly funded by Coordenação de Aperfeiçoamento de Pessoal de Nível Superior (CAPES), Fundação de Amparo à Pesquisa do Estado de São Paulo (FAPESP grants: 2015/15027-7 and 2016/22011-2), and Conselho Nacional de Desenvolvimento Científico e Tecnológico (CNPq grants 304674/2014-1 and 429885/2016-4). The authors are grateful to UCAR (United States) and NSPO (Taiwan) for providing and processing the FORMOSAT-3/COSMIC RO data (http://cdaac-www.cosmic.ucar.edu/), to MIT/Haystack Observatory for providing the ISR data at the Madrigal database (http://madrigal.haystack.mit.edu/), and to the IRI model (https://iri.gsfc.nasa.gov/) due to the neutral temperature computations. Also, the GEC data are available and they can be requested from any of the authors, in particular, to Fabricio S. Prol (fabricioprol@hotmail.com) and Manuel Hernàndez-Pajares (manuel.hernandez@upc.edu).

References

Belehaki, A., Marinov, P., Kutiev, I., Jakowski, N., & Stankov, S. (2006). Comparison of the topside ionosphere scale height determined by topside sounders model and bottomside digisonde profiles. *Advances in Space Research*, *37*, 963–966.

Bilitza, D., McKinnel, L. A., Reinisch, B., & Fuller-Rowell, T. (2011). The international reference ionosphere today and in the future. *Journal of Geodesy*, *85*, 909–920.

Chapman, S. (1931). The absorption and dissociative or ionizing effect of monochromatic radiation in an atmosphere on a rotating Earth. *Proceedings of the Physical Society*, *43*, 26–45.

Depuev, V. H., & Pulinets, S. A. (2004). A global empirical model of the ionospheric topside electron density. *Advances in Space Research*, *34*, 2016–2020.

Duarte-Silva, M. H., Muella, M. T. A. H., Silva, L. C. C., Abreu, A. J., & Fagundes, P. R. (2015). Ionospheric slab thickness at the equatorial anomaly region after the deep solar minimum of cycle 23/24. *Advances in Space Research*, *56*, 1961–1972. https://doi.org/10.1016/j.asr.2015.05.010

Fonda, C., Coisson, P., Nava, B., & Radicella, S. M. (2005). Comparison of analytical functions used to describe topside electron density profiles with satellite data. *Annales Geophysicae*, *48*, 491–495.

Hernández-Pajares, M., Garcia-Fernàndez, M., Rius, A., Notarpietro, R., von Engeln, A., & Olivares-Pulido, G. (2017). Electron density extrapolation above F_2 peak by the linear Vary-Chap model supporting new Global Navigation Satellite Systems-LEO occultation missions. *Journal of Geophysical Research: Space Physics*, *122*, 9003–9014. https://doi.org/10.1002/2017JA023876

Hernández-Pajares, M., Juan, J. M., & Sanz, J. (1999). New approaches in global ionospheric determination using ground GPS data. *Journal of Atmospheric and Solar-Terrestrial Physics*, *61*, 1237–1247.

Kelley, M. C. (2009). *The Earth's ionosphere: Plasma physics and electrodynamics* (2nd ed.). New York: Academic Press.

Kutiev, I., & Marinov, P. (2007). Topside sounder model of scale height and transition height characteristics of the ionosphere. *Advances in Space Research*, *39*, 759–766.

Lei, J., Syndergaard, S., Burns, A. G., Solomon, S. C., Wang, W., Zeng, Z., et al. (2007). Comparison of COSMIC ionospheric measurements with ground-based observations and model predictions: Preliminary results. *Journal of Geophysical Research*, *112*, A07308. https://doi.org/10.1029/2006JA012240

Liu, L., Le, H., Chen, Y., He, M., Wan, W., & Yue, X. (2011). Features of the middle- and low-latitude ionosphere during solar minimum as revealed from COSMIC radio occultation measurements. *Journal of Geophysical Research*, *116*, A09307. https://doi.org/10.1029/2011JA016691

Llewellyn, S. K., & Bent, R. B. (1973). Documentation and description of the Bent Ionospheric Model (Report AFCRL-TR-73-0657). Mass: Hanscom AFB.

Marinov, P., Kutiev, I., Belehaki, A., & Tsagouri, I. (2015). Modeling the plasmasphere to topside ionosphere scale height ratio. *Journal of Space Weather and Space Climate*, *5*, A27. https://doi.org/10.1051/swsc/2015028

Olivares-Pulido, G., Hernández-Pajares, M., Aragón-Angel, A., & Garcia-Rigo, A. (2016). A linear scale height Chapman model supported by GNSS occultation measurements. *Journal of Geophysical Research: Space Physics*, *121*, 7932–7940. https://doi.org/10.1002/2016JA022337

Pedatella, N. M., Forbes, J. M., Maute, A., Richmond, A. D., Fang, T.-W., Larson, K. M., & Millward, G. (2011). Longitudinal variations in the *F* region ionosphere and the topside ionosphere-plasmasphere: Observations and model simulations. *Journal of Geophysical Research*, *116*, A12309. https://doi.org/10.1029/2011JA016600

Prol, F. S., & Camargo, P. O. (2016). Ionospheric tomography using GNSS: multiplicative algebraic reconstruction technique applied to the area of Brazil. *GPS Solutions*, *20*, 807–814. https://doi.org/10.1007/s10291-015-0490-0

Rawer, K. (1988). Synthesis of ionospheric electron density profiles with Epstein functions. *Advances in Space Research*, *8*, 191–198.

Radicella, S. M., & Leitinger, R. (2001). The evolution of the DGR approach to model electron density profiles. *Advances in Space Research*, *27*, 35–40. https://doi.org/10.1016/S0273-1177(00)00138-1

Reinisch, B. W., Huang, X., Belehaki, A., Shi, J., Zhang, M. L., & Ilma, R. (2004). Modeling the IRI topside profile using scale heights from ground-based ionosonde measurements. *Advances in Space Research*, *34*, 2026–2031. https://doi.org/10.1016/j.asr.2004.06.012

Rishbeth, H., & Garriott, O. K. (1969). *Introduction to ionospheric physics*. New York: Academic Press.

Reinisch, B. W., Nsumei, P., Huang, X., & Bilitza, D. K. (2007). Modeling the F2 topside and plasmasphere for IRI using IMAGE/RPI, and ISIS data. *Advances in Space Research*, *39*, 731–738. https://doi.org/10.1016/j.asr.2006.05.032

Schreiner, W. S., Sokolovskiy, S. V., Rocken, C., & Hunt, D. C. (1999). Analysis and validation of GPS/MET radio occultation data in the ionosphere. *Radio Science*, *34*, 949–966.

Stankov, S. M., & Jakowski, N. (2006). Topside ionospheric scale height analysis and modeling based on radio occultation measurements. *Journal of Atmospheric and Solar-Terrestrial Physics*, *68*, 134–162.

Stankov, S. M., Jakowski, N., Heise, S., Muhtarov, P., Kutiev, I., & Warnant, R. (2003). A new method for reconstruction of the vertical electron density distribution in the upper ionosphere and plasmasphere. *Journal of Geophysical Research*, *108*, 1164. https://doi.org/10.1029/2002JA009570

Syndergaard, S., Kursinski, E. R., Herman, B. M., Lane, E. M., & Flittner, D. E. (2005). A refractive index mapping operator for assimilation of occultation data. *Monthly Weather Review*, *133*, 2650–2668.

Venkatesh, K., Rama Rao, P. V. S., Saranya, P. L., Prasad, D. S. V. V. D., & Niranjan, K. (2011). Vertical electron density and topside effective scale height (HT) variations over the Indian equatorial and low latitude stations. *Annales Geophysicae*, *29*, 1861–1872.

Wu, M. J., Guo, P., Fu, N. F., Xu, T. L., Xu, X. S., Jin, H. L., & Hu, X. G. (2016). Topside correction of IRI by global modeling of ionospheric scale height using COSMIC radio occultation data. *Journal of Geophysical Research: Space Physics*, *121*, 5675–5692. https://doi.org/10.1002/2016JA022785

Zhao, B., Wan, W., Yue, X., Liu, L., Ren, Z., He, M., & Liu, J. (2011). Global characteristics of occurrence of an additional layer in the ionosphere observed by COSMIC/FORMOSAT-3. *Geophysical Research Letters*, *38*, L02101. https://doi.org/10.1029/2010GL045744